

Sm-Nd Isotope Data Compilation from Geoscientific Literature Using an Automated Tabular Extraction Method

Zhixin Guo¹, Tao Wang², Chaoyang Wang², Jianping Zhou¹, Guanjie Zheng^{3,*}, Xinbing Wang¹, and Chenghu Zhou⁴

¹Shanghai Jiao Tong University, School of Electronic Information and Electrical Engineering, Shanghai, 200240, China

²Chinese Academy of Geological Sciences, Institute of Geology, Beijing, 100037, China

³Shanghai Jiao Tong University, John Hopcroft Center for Computer Science, Shanghai, 200240, China

⁴Chinese Academy of Sciences, Institute of Geological Sciences and Natural Resources Research, Beijing, 100101, China

*corresponding author(s): Guanjie Zheng (gjzheng@sjtu.edu.cn)

ABSTRACT

The rare earth elements Sm and Nd significantly address fundamental questions about crustal growth, such as its spatiotemporal evolution and the interplay between orogenesis and crustal accretion. Their relative immobility during high-grade metamorphism makes the Sm-Nd isotopic system crucial for inferring crustal formation times. Historically, data have been disseminated sporadically in the scientific literature due to complicated and costly sampling procedures, resulting in a fragmented knowledge base. However, the scattering of critical geoscience data across multiple publications poses significant challenges regarding human capital and time. In response, we present an automated tabular extraction method for harvesting tabular geoscience data. We collect 10,624 Sm-Nd data entries from 9,138 tables in over 20,000 geoscience publications using this method. We manually selected 2,118 data points from it to supplement our previously constructed global Sm-Nd dataset, increasing its sample count by over 20%. Our automatic data collection methodology enhances the efficiency of data acquisition processes spanning various scientific domains. Furthermore, the constructed Sm-Nd isotopic dataset should motivate the research of classifying global orogenic belts.

1 Background & Summary

In igneous science, it is critical to efficiently collect spatial, temporal, and geochemical data from myriad samples. Such data play a prominent role in understanding high-level geological phenomena such as reconstructing ancient plate kinematics, delineating processes of continental convergence and dispersal, assessing crustal growth, and investigating the deep material structure of orogens¹⁻⁷. Determining the formation time of continental crustal protoliths within metamorphic terrains is a significant challenge. This complexity is primarily due to the fluctuating effects of tectonothermal events on isotopic systems. Such events can lead to redistributing parent-daughter elements and consequently to partial or complete re-equilibration of isotopic systems on scales ranging from individual minerals to entire outcrops. In particular, Sm and Nd are often considered relatively immobile during high-grade metamorphism^{8,9}. As a result, the Sm-Nd isotopic system has been used extensively to derive ages ranging from the most recent metamorphic events to the original formation of the crust¹⁰⁻¹³. Groundbreaking studies have highlighted the importance of the Sm-Nd isotope. These studies have investigated the provenance and petrogenesis of igneous rocks^{14,15}, identified allochthonous terranes within orogens¹⁶⁻¹⁸, and investigated the dynamics of continental crustal growth^{3,19-24}. Compilations of Sm-Nd isotope datasets have proven to be invaluable repositories, providing insights into historical and contemporary states of global systems and offering predictions of future conditions. Orogens, the foundations of plate tectonics, are primarily composite structures that undergo myriad phases of orogeny.

Despite its potential, synthesizing Sm-Nd isotope data, which spans vast spatial and temporal dimensions and cuts across diverse scientific landscapes, presents formidable challenges. These arise primarily from the nuanced processes required to extract large datasets from various scientific publications efficiently. By their very nature, geoscience data are besieged by a number of obstacles, from the pitfalls of non-reproducibility and inherent uncertainties to the challenges posed by their multifaceted nature, massive computational demands, and the need for cyclical updates²⁵. In the burgeoning era of big data, the international geoscience community is grappling with an unprecedented surge in the volume and complexity of data structures^{26,27}. Traditional methods, which rely primarily on manual data collection and categorization, need to be revised

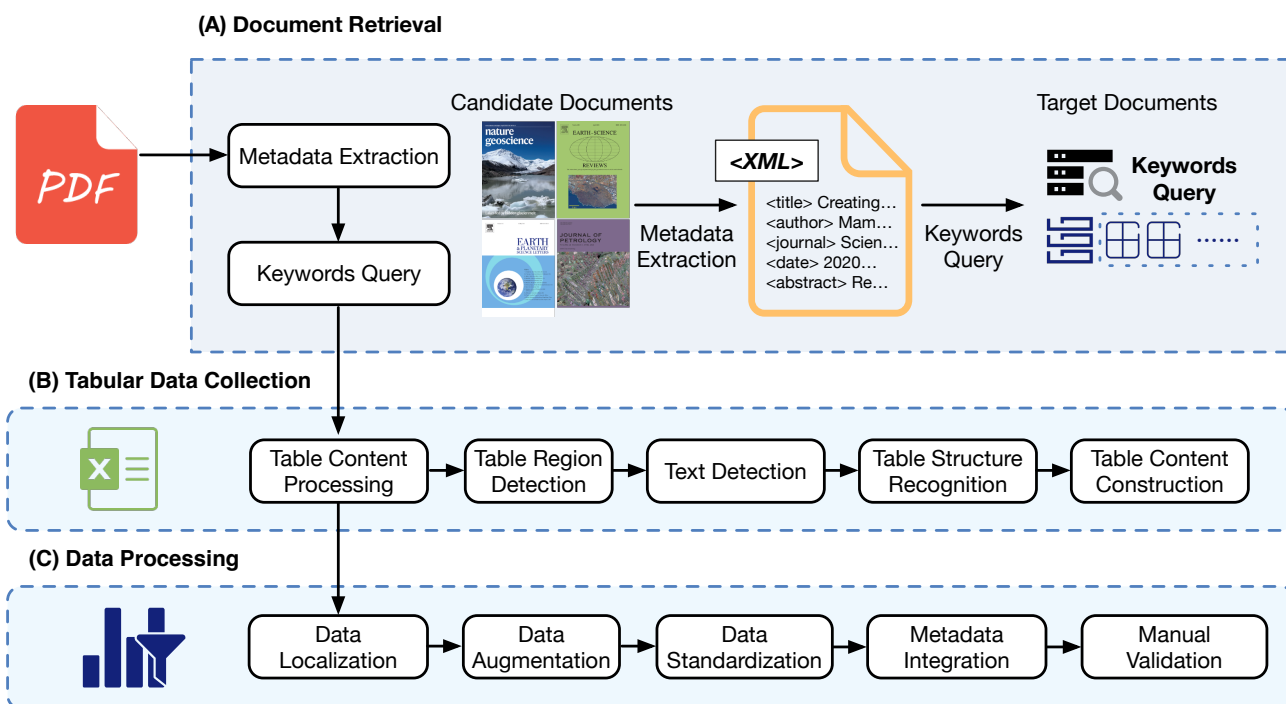


Figure 1. An overview of the automatic searching and collecting tabular data tool workflow, which consists of two main steps: (A) document retrieval and (B) tabular data collection.

when confronted with the colossal repositories of information and the multifaceted challenges of data archival review^{28–30}. Despite the increased emphasis that modern magmatic databases place on both the volume and integrity of their samples, the effectiveness of data collection strategies remains underexplored^{31,32}.

With the advent of neural network-based techniques, there has been a marked alleviation in the challenges associated with analyzing vast textual data. A significant trend has emerged wherein there is an inclination toward deciphering elements and extracting semantic content from PDF documents. The techniques propelling these advancements can be bifurcated into two primary domains: methods anchored in visual analysis^{33–35} and those founded on pre-trained language models (PLMs)^{36–40}. Both approaches have showcased noteworthy efficacy in their designated domains. Notwithstanding, it is pivotal to note that these techniques predominantly concentrate on visual element recognition or deeply engage with natural language processing (NLP) in end-to-end networks. Although proficient within their respective scopes, such specialization may not fully cater to the burgeoning demand for swift and exhaustive data extraction from intricate tabular formats. Historically, methodologies, as exemplified by platforms like Chronos⁴¹, GeoSciNet⁴², GeoDeepDive⁴³, SciSpace⁴⁴, and GeoDeepShovel⁴⁵, have leaned on neural network paradigms explicitly tailored for scientific literature analysis. However, despite their significant contributions, most of these methods are predominantly tailored for single-document analysis, consequently constraining their applicability to data extraction from individual documents.

In light of this limitation, we present an innovative approach, illustrated in Figure 1, that bifurcates the process into two core modules: document retrieval and tabular data aggregation. Unlike these efforts in geoscience data aggregation^{46–49}, our approach provides a more cohesive workflow that seamlessly integrates document retrieval and tabular data collection. Such integration dramatically increases the efficiency of data acquisition from geoscience repositories. Using this tool, we obtained 10,624 Sm-Nd datasets from 9,138 tables spanning more than 20,000 geoscience articles. Extensive curation of this vast repository resulted in 2,118 meticulously curated datasets, adding over 20% to our global Sm-Nd compendium.

2 Methods

2.1 Document Retrieval

Figure 1(A) illustrates the core components of our PDF parsing protocol, which integrates metadata extraction and advanced keyword querying techniques. The beginning of our process is anchored in the meticulous extraction of metadata from a curated selection of PDF documents. In this phase, we use CERMINE⁵⁰, an automatic tool equipped with precision to extract structured metadata from various scientific publications. This instrumental phase ensures a comprehensive and accurate capture of key

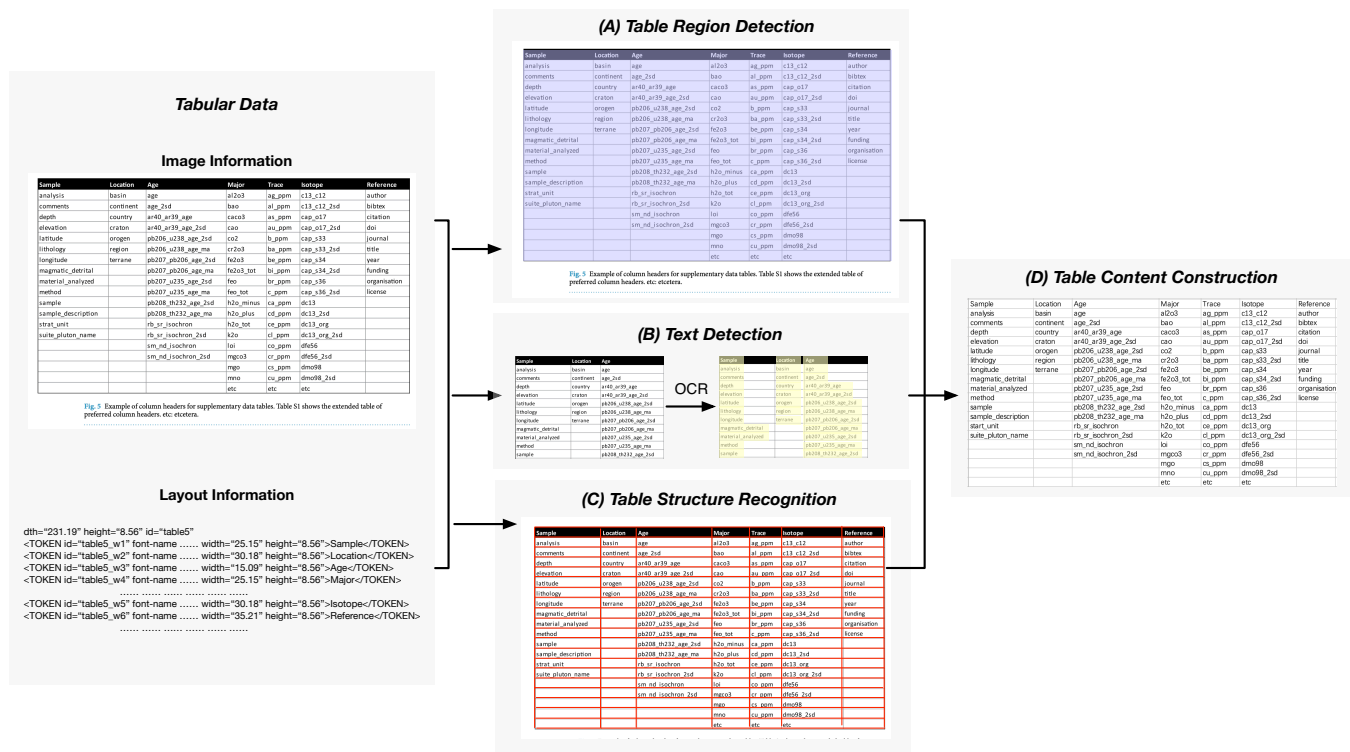


Figure 2. An overview of tabular data collection pipeline. The pipeline process consists of four modules: (a) table region detection, (b) text detection, (c) table structure recognition, and (d) table content construction.

metadata components, including but not limited to title, authorship, abstract, affiliations, included keywords, and intricate bibliographic specifics (including journal name, volume, issue, and DOI). A notable feature of CERMINE is its ability to capture the rich content structure, encapsulating textual narratives, segmented sections, illustrative figures, tabular data, and accompanying captions while preserving the integrity of layout specifics and element positions. The captured metadata is then transformed into XML documents to facilitate an enhanced scheme of analytical review and organizational refinement.

The following phase is characterized by optimizing the keyword query efficiency, which is realized by implementing a multifaceted data transformation protocol. Integral to this process is the conversion of all tokens to lowercase, the substitution of spaces for non-alphanumeric characters, the elimination of common stop words, and the expansion of standard abbreviations, culminating in a standardized and normalized data set that enhances consistency and comparative accuracy in subsequent phases of data retrieval. In the context of our focus study on Sm-Nd isotopes, a meticulously constructed keyword matrix, described in Table 1, coupled with specialized filtering rules, enhances the precision and speed of target document identification and extraction.

1. Inclusion criteria include terms such as ϵNd , Sm-Nd, Sm-Nd-Hf, $^{143}\text{Nd}/^{144}\text{Nd}$, Nd isotope, or TDM in the title or abstract.
2. The criteria further extend to the inclusion of terms related to geological and mineralogical descriptors, including felsic, granite, granitic, pluton, plutonic, magmatic, magma, diorite, or rhyolite, in the title or abstract.

Our methodology culminates in selecting scholarly articles that meet the two enumerated criteria, ensuring a comprehensive and targeted inclusion of documents intrinsically aligned with our study's thematic and conceptual underpinnings. This multifaceted approach underscores a synthesis of methodological rigor and technological sophistication, embodying a blueprint for enhanced accuracy and efficiency in extracting and analyzing complex scientific data.

2.2 Tabular Data Collection

Figure 2 illustrates the pipeline we developed for extracting tabular data from PDF documents, a complex task due to the heterogeneous nature of these files. The elaborated strategy is based on three key stages: table region detection, table structure recognition, and nuanced table content construction. A notable challenge in this endeavor is a universal encoding standard for PDF files. This gap leads to problems, particularly the appearance of garbled text, which leads to omitting essential layout

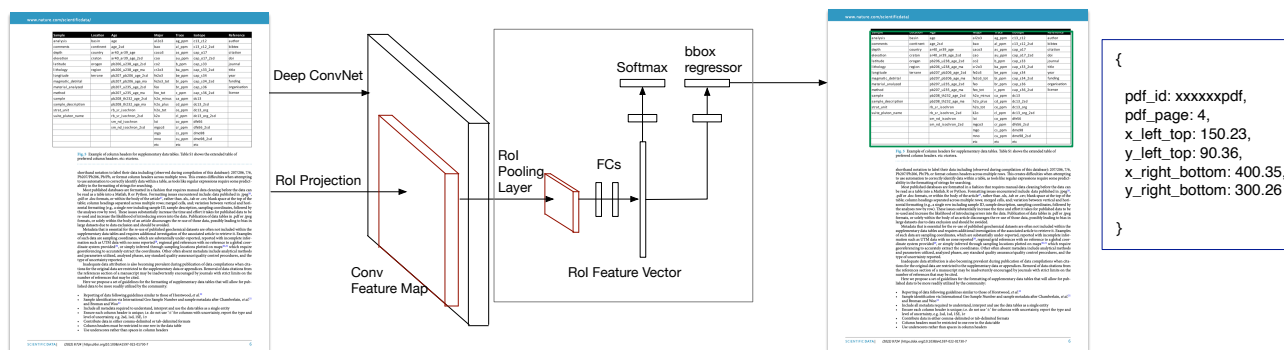


Figure 3. An overview of table region detection processing. The table detection neural network localize tables and returns the table position and page information.

information. We address this challenge by converting each page of tabular data to images. We then employ a computer vision (CV)-based methodology to increase the recognition accuracy for table construction.

Sample	Nation	Region	GeoTectonic unit	Groups
Tectonic unit	Subtectonic unit	Sub groups	Longitude	Latitude
Lithology	Pluton	Formation	Age (Ma)	Sm
Nd	147Sm/144Nd	143Nd/144Nd	2 σ	$f_{Sm/Nd}$
ϵ Nd	TDM1	TDM2	Author	Year
Journal	Title	Volume	Page	DOI

Table 1. Keyword list for document identification and extraction.

2.2.1 Table Region Detection

Our table region detection model was developed using Fast Region-based Convolutional Network (Fast R-CNN)⁵¹, a machine learning algorithm acclaimed for its accuracy and efficiency. Fast R-CNN is instrumental in accurately identifying and precisely localizing table regions in various documents. The model’s effectiveness is further enhanced by its training on TableBank⁵², a robust and comprehensive dataset curated explicitly to refine table detection algorithms. Our model demonstrated 97% accuracy on the TableBank dataset throughout the training phase.

As a practical application of the refined model, we set out to identify tables embedded in academic PDFs. Using PDF parsing techniques, we extract metadata to detect the presence of embedded table tags within document pages. When such tags are detected, the corresponding pages are converted to images, setting the stage for more granular analysis. Figure 3 presents an overview of table region detection processing. The Table Detection Neural Network then analyzes each image to identify and localize tables accurately. In cases where the network confirms the presence of a table, it not only returns the specific page number but also pinpoints the exact relative position of the table frame on that page.

2.2.2 Text Detection

Our methodology begins with an assessment to determine if the PDF pages with tables have an accompanying text layer. In cases where this layer is missing, we employ easyOCR⁵³, a reputable Optical Character Recognition (OCR) tool celebrated for its precision and efficiency, to introduce a text layer. This addition ensures that the text aligns accurately with its corresponding positions in the image. Once integrated, we meticulously organize the text layer to maintain visual and structural integrity. Subsequently, an exhaustive inventory of text dimensions across the entire PDF document is prepared, offering an in-depth analysis of text characteristics.

The average text width, derived from this inventory, is instrumental in estimating text spacing - a critical parameter in our study. This estimated text spacing is not merely a numerical value but serves as a cornerstone for deciphering the intricate structure of embedded tables within the document. It plays a pivotal role in enhancing the accuracy and efficiency of table extraction and analysis, thus contributing profoundly to the rigor and precision of our research outcomes.

Marker	Monitoring Device	Frequency
(A)	Sleep Tracking Mat	Every minute
In-home movement	PIR and Door Sensors	Continuous from multiple locations (precision in seconds)
Body/Skin Temperature	Thermometer	Continuous in a short period per day (precision in seconds)
Diastolic/Systolic Blood Pressure	BPM Connect	Once a day
Heart Rate	Heart Rate	Once a day
Muscle Mass/Body Weight/Total Body Water	Smart Scale	Once a day

Table 1. Overview of the digital markers collected in the TIHM dataset¹⁰, detailing the monitoring device used and the frequency of measurement for the collection of data.

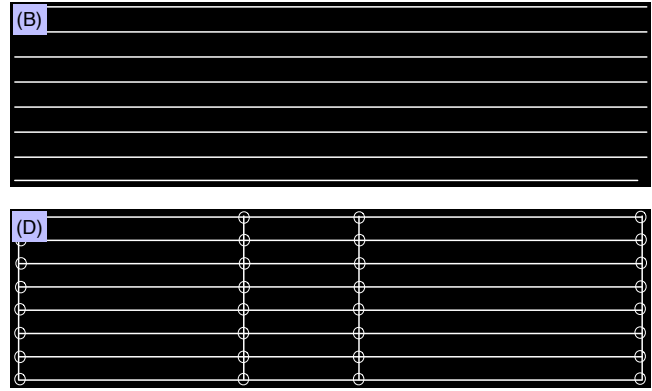


Figure 4. An overview of tabular structure recognition with frames. (A) denotes the initial table structure complete with frames. (B) indicates the detection of horizontal lines. (C) indicates the vertical line detection, and (D) showcases the identification of adjacent points.

2.2.3 Table Structure Recognition

To accurately delineate sections within tables, our first approach is to capture images of tables, focusing on their outer borders and relative position within a PDF document. The images are then subjected to a sophisticated pre-processing stage. Each input image is first converted to grayscale, followed by adaptive thresholding for binarization. Morphological operations, namely image erosion and dilation, are then applied to identify vertical and horizontal lines. This meticulous process separates text and boundary lines while eliminating unnecessary noise. During the post-processing phase, we categorize table morphologies to determine the presence or absence of internal borderlines. This determination depends on detecting vertical and horizontal lines within the table. A pixel count that exceeds a predetermined threshold indicates the presence of these internal border lines. As shown in Figure 4, we assiduously extract both vertical and horizontal lines, noting intersection points where they exist. Any superfluous intersections are methodically pruned, resulting in a streamlined set of internal frame intersection coordinates. We assess whether adjacent points connect to form internal frame lines using this refined dataset. These connections are established during validation, culminating in a structural representation that highlights tables equipped with internal frame lines.

On the other hand, as shown in Figure 5, for tables that do not have internal frame lines, our methodology focuses on their identification by analyzing the maximum connected intervals between texts. The procedure includes the following steps, ensuring a comprehensive approach to the extraction of complex tabular structures:

- **Image Processing.** The input image is first converted to grayscale in the preliminary image preprocessing stage. Adaptive thresholding is then applied to achieve binarization. Subsequent operations include applying morphological techniques, specifically image erosion and dilation, to identify vertical and horizontal lines. Lines exceeding a certain length, determined by a predefined threshold, are systematically eliminated. After these steps, the image is subjected to another thresholding process that normalizes the pixel values: the values are set to 0 for blank areas and 255 for areas populated with text. This process ensures optimal contrast and improved clarity within the image.
- **Horizontal Frame Lines Identification.** We use a systematic pixel-by-pixel scan from top to bottom of the image. Rows with a pixel value sum of zero are marked as potential zones containing horizontal internal frame lines. By merging all adjacent potential zones and locating the midpoints of these continuous zero-value regions, we derive the precise locations of the internal frame lines that segment rows within the table.
- **Vertical Frame Lines Identification.** A sequential vertical scan is performed between adjacent horizontal internal frame lines. Each column’s summation of pixel values facilitates the distinction between text and blank areas. We merge contiguous blank areas that are vertically aligned and eliminate those that are the height of a single line. The vertical lines that intersect the largest cumulative blank areas are designated as the vertical internal frame lines of the table, with each iteration marking the intersecting areas as traversed until all blank areas are accounted for.
- **Table Structure Recognition.** The intersection of the border and the vertical inner border lines delineates the primary unit cells of the table. Each cell’s vertical lines are carefully examined to determine their intersection with text-containing zones. Segments of vertical lines that intersect text are excised, resulting in a horizontal merging of cells. This rigorous process reveals the table’s refined internal frame line structure after cell merging.

(A)	Assimilation-fractional crystallization				Assimilation-fractional crystallization						
	Parent		Contaminant		R=0.3		R=0.5				
	D	PL9	C2	20	40	60	80	20	40	60	80
Rb	0.2	50	64	65	89	131	238	72	106	164	301
Sr	1.03	812	874	824	837	854	877	832	853	874	895
Ba	0.34	1047	779	1253	1556	2066	3225	1304	1664	2230	3384
K ₂ O	0.63	2.08	1.92	2.31	261	3.1	3.87	2.38	2.74	3.2	3.88
Ce	0.53	76.4	73.1	88	104	128	176	92	111	138	183
Nd	0.85	34.5	31.7	36.4	38.8	41.9	46.7	37.3	40.4	43.8	47.8
Eu	1.38	1.97	1.66	1.73	1.49	1.24	1	1.64	1.36	1.15	1.01
Yb	0.97	1.56	1.53	1.57	1.59	1.6	1.63	1.57	1.59	1.6	1.62
Lu	0.92	0.231	0.226	0.236	0.242	0.25	0.261	0.237	0.244	0.251	0.259
Y	0.6	18.1	17.8	20.4	23.6	28.2	36.8	21.2	25.1	30.1	37.9
TO ₂	0.89	0.91	0.71	0.92	0.94	0.96	0.98	0.91	0.91	0.91	0.91
Zr	0.31	79	147	104	142	206	356	120	179	272	470
Hf	0.31	2.1	3.6	2.7	3.7	5.3	9.1	3.1	4.6	6.9	11.8
Nb	0.47	5.1	6.1	6.1	7.5	9.7	14.2	6.5	8.4	11.1	15.9
Th	0.3	1.45	5.59	2.22	3.37	5.35	10.03	2.89	4.96	8.32	15.5
U	0.06	0.45	1.43	0.7	1.12	1.91	4.19	0.9	1.62	3.01	6.89
Co	1.17	114	100	107	100	91	81	104	95	86	79

(B)	Assimilation-fractional crystallization				Assimilation-fractional crystallization						
	Parent		Contaminant		R=0.3		R=0.5				
	D	PL9	C2	20	40	60	80	20	40	60	80
Rb	0.2	50	64	65	89	131	238	72	106	164	301
Sr	1.03	812	874	824	837	854	877	832	853	874	895
Ba	0.34	1047	779	1253	1556	2066	3225	1304	1664	2230	3384
K ₂ O	0.63	2.08	1.92	2.31	261	3.1	3.87	2.38	2.74	3.2	3.88
Ce	0.53	76.4	73.1	88	104	128	176	92	111	138	183
Nd	0.85	34.5	31.7	36.4	38.8	41.9	46.7	37.3	40.4	43.8	47.8
Eu	1.38	1.97	1.66	1.73	1.49	1.24	1	1.64	1.36	1.15	1.01
Yb	0.97	1.56	1.53	1.57	1.59	1.6	1.63	1.57	1.59	1.6	1.62
Lu	0.92	0.231	0.226	0.236	0.242	0.25	0.261	0.237	0.244	0.251	0.259
Y	0.6	18.1	17.8	20.4	23.6	28.2	36.8	21.2	25.1	30.1	37.9
TO ₂	0.89	0.91	0.71	0.92	0.94	0.96	0.98	0.91	0.91	0.91	0.91
Zr	0.31	79	147	104	142	206	356	120	179	272	470
Hf	0.31	2.1	3.6	2.7	3.7	5.3	9.1	3.1	4.6	6.9	11.8
Nb	0.47	5.1	6.1	6.1	7.5	9.7	14.2	6.5	8.4	11.1	15.9
Th	0.3	1.45	5.59	2.22	3.37	5.35	10.03	2.89	4.96	8.32	15.5
U	0.06	0.45	1.43	0.7	1.12	1.91	4.19	0.9	1.62	3.01	6.89
Co	1.17	114	100	107	100	91	81	104	95	86	79

(C)	Assimilation-fractional crystallization				Assimilation-fractional crystallization						
	Parent		Contaminant		R=0.3		R=0.5				
	D	PL9	C2	20	40	60	80	20	40	60	80
Rb	0.2	50	64	65	89	131	238	72	106	164	301
Sr	1.03	812	874	824	837	854	877	832	853	874	895
Ba	0.34	1047	779	1253	1556	2066	3225	1304	1664	2230	3384
K ₂ O	0.63	2.08	1.92	2.31	261	3.1	3.87	2.38	2.74	3.2	3.88
Ce	0.53	76.4	73.1	88	104	128	176	92	111	138	183
Nd	0.85	34.5	31.7	36.4	38.8	41.9	46.7	37.3	40.4	43.8	47.8
Eu	1.38	1.97	1.66	1.73	1.49	1.24	1	1.64	1.36	1.15	1.01
Yb	0.97	1.56	1.53	1.57	1.59	1.6	1.63	1.57	1.59	1.6	1.62
Lu	0.92	0.231	0.226	0.236	0.242	0.25	0.261	0.237	0.244	0.251	0.259
Y	0.6	18.1	17.8	20.4	23.6	28.2	36.8	21.2	25.1	30.1	37.9
TO ₂	0.89	0.91	0.71	0.92	0.94	0.96	0.98	0.91	0.91	0.91	0.91
Zr	0.31	79	147	104	142	206	356	120	179	272	470
Hf	0.31	2.1	3.6	2.7	3.7	5.3	9.1	3.1	4.6	6.9	11.8
Nb	0.47	5.1	6.1	6.1	7.5	9.7	14.2	6.5	8.4	11.1	15.9
Th	0.3	1.45	5.59	2.22	3.37	5.35	10.03	2.89	4.96	8.32	15.5
U	0.06	0.45	1.43	0.7	1.12	1.91	4.19	0.9	1.62	3.01	6.89
Co	1.17	114	100	107	100	91	81	104	95	86	79

(D)	Assimilation-fractional crystallization				Assimilation-fractional crystallization						
	Parent		Contaminant		R=0.3		R=0.5				
	D	PL9	C2	20	40	60	80	20	40	60	80
Rb	0.2	50	64	65	89	131	238	72	106	164	301
Sr	1.03	812	874	824	837	854	877	832	853	874	895
Ba	0.34	1047	779	1253	1556	2066	3225	1304	1664	2230	3384
K ₂ O	0.63	2.08	1.92	2.31	261	3.1	3.87	2.38	2.74	3.2	3.88
Ce	0.53	76.4	73.1	88	104	128	176	92	111	138	183
Nd	0.85	34.5	31.7	36.4	38.8	41.9	46.7	37.3	40.4	43.8	47.8
Eu	1.38	1.97	1.66	1.73	1.49	1.24	1	1.64	1.36	1.15	1.01
Yb	0.97	1.56	1.53	1.57	1.59	1.6	1.63	1.57	1.59	1.6	1.62
Lu	0.92	0.231	0.226	0.236	0.242	0.25	0.261	0.237	0.244	0.251	0.259
Y	0.6	18.1	17.8	20.4	23.6	28.2	36.8	21.2	25.1	30.1	37.9
TO ₂	0.89	0.91	0.71	0.92	0.94	0.96	0.98	0.91	0.91	0.91	0.91
Zr	0.31	79	147	104	142	206	356	120	179	272	470
Hf	0.31	2.1	3.6	2.7	3.7	5.3	9.1	3.1	4.6	6.9	11.8
Nb	0.47	5.1	6.1	6.1	7.5	9.7	14.2	6.5	8.4	11.1	15.9
Th	0.3	1.45	5.59	2.22	3.37	5.35	10.03	2.89	4.96	8.32	15.5
U	0.06	0.45	1.43	0.7	1.12	1.91	4.19	0.9	1.62	3.01	6.89
Co	1.17	114	100	107	100	91	81	104	95	86	79

(E)	Assimilation-fractional crystallization								Assimilation-fractional crystallization			
	R=0.3				R=0.5				R=0.5			
	Parent		Contaminant		R=0.3		R=0.5		R=0.5		R=0.5	
Elements	D	PL9	C2	20	40	60	80	20	40	60	80	
Rb	0.2	50	64	65	89	131	238	72	106	164	301	
Sr	1.03	812	874	824	837	854	877	832	853	874	895	
Ba	0.34	1047	779	1253	1556	2066	3225	1304	1664	2230	3384	
K ₂ O	0.63	2.08	1.92	2.31	261	3.1	3.87	2.38	2.74	3.2	3.88	
Ce	0.53	76.4	73.1	88	104	128	176	92	111	138	183	
Nd	0.85	34.5	31.7	36.4	38.8	41.9	46.7	37.3	40.4	43.8	47.8	
Eu	1.38	1.97	1.66	1.73	1.49	1.24	1	1.64	1.36	1.15	1.01	
Yb	0.97	1.56	1.53	1.57	1.59	1.6	1.63	1.57	1.59	1.6	1.62	
Lu	0.92	0.231	0.226	0.236	0.242	0.25	0.261	0.237	0.244	0.251	0.259	
Y	0.6	18.1	17.8	20.4	23.6	28.2	36.8	21.2	25.1	30.1	37.9	
TO ₂	0.89	0.91	0.71	0.92	0.94	0.96	0.98	0.91	0.91	0.91	0.91	
Zr	0.31	79	147	104	142	206	356	120	179	272	470	
Hf	0.31	2.1	3.6	2.7	3.7	5.3	9.1	3.1	4.6	6.9	11.8	
Nb	0.47	5.1	6.1	6.1	7.5	9.7	14.2	6.5	8.4	11.1	15.9	
Th	0.3	1.45	5.59	2.22	3.37	5.35	10.03	2.89	4.96	8.32	15.5	
U	0.06	0.45	1.43	0.7	1.12	1.91	4.19	0.9	1.62	3.01	6.89	
Co	1.17	114	100	107	100	91	81	104	95	86	79	

Figure 5. An overview of tabular structure recognition without frames. (A) presents the initial table lacking frames. (B) illustrates the result of image processing. (C) exhibits the construction of vertical and horizontal lines. (D) indicates the table structure post-cell merging recognition. (E) displays the final output following comprehensive table structure recognition.

This systematic methodology ensures accurate and efficient identification and extraction of table structures, especially those without explicit internal boundaries, by analyzing and processing the interconnectedness of text intervals and boundaries.

2.2.4 Table Content Construction

Using the reconstructed internal border structure of the table, we determine the rectangular frame coordinates for each cell within the PDF document. We then extract text information from coincident areas of the PDF text layer. After eliminating and adjusting for spaces, we determine the exact content of the table cell. By integrating the internal border lines and the corresponding cell contents, we construct an Excel spreadsheet, ensuring that the data associated with the merged cells is meticulously documented and preserved.

2.3 Data Processing

After extracting the tabular data, we embarked on a rigorous data processing regimen concentrating on the Sm-Nd isotope data. The procedural steps included the following methods:

- **Data Localization.** The initial step is to locate the table that contains the Sm and Nd ratio, uniquely defined as the $^{147}\text{Sm}/^{144}\text{Nd}$ field. This preliminary stage allows the extraction of the Sm-Nd isotope data from the current literature, supplemented by its unique identifier, referred to as the Sample ID.
- **Data Augmentation.** It is worth noting that the extracted sample data often lacks several key fields, resulting in a remarkably sparse dataset. Based on the sample number derived from the previous step, additional searches are performed in other tables to enrich specific fields, such as the geographic coordinates of the sample. In cases where certain fields remain empty, the title and abstract of the literature are examined according to predefined protocols to retrieve and embed potentially correlating data.
- **Data Standardization.** Building on the initial data obtained, it was imperative to implement a data normalization process specifically for the key datasets. This adjustment not only supports easy data categorization and interpretation but also paves the way for intensive exploration of the assimilated data. Recalculated measures not only allow for a unified parameter-based data conversion but also enhance the robustness of the dataset, ensuring its consistency with the original literature data, thereby solidifying the credibility of the derived data.

For the computation of Nd values, we adopted the chondritic standards, precisely $(^{143}\text{Nd}/^{144}\text{Nd})_{\text{CHUR}} = 0.512638$, $(^{147}\text{Sm}/^{144}\text{Nd})_{\text{CHUR}} = 0.1967159^{54}$, $(^{143}\text{Nd}/^{144}\text{Nd})_{\text{DM}} = 0.51315$, and $(^{147}\text{Sm}/^{144}\text{Nd})_{\text{DM}} = 0.21372$, as representative of the contemporary Depleted mantle^{55,56}.

The analytical process focuses on the calculation of three primary standardized parameters, including ϵ_{Nd} , T_{DM1} , and T_{DM2} . These are derived according to the following mathematical formulations⁵⁷:

$$\epsilon_{\text{Nd}} = \frac{(^{143}\text{Nd}/^{144}\text{Nd})_{\text{sample (T)}}}{(^{143}\text{Nd}/^{144}\text{Nd})_{\text{CHUR(T)}} - 1} \times 10000 \quad (1)$$

$$T_{\text{DM1}} = 1/\lambda \times \ln \left(1 + \frac{(^{143}\text{Nd}/^{144}\text{Nd})_{\text{sample (T)}} - 0.51315}{(^{147}\text{Sm}/^{144}\text{Nd})_{\text{sample (T)}} - 0.2137} \right) \quad (2)$$

$$T_{\text{DM2}} = \frac{T_{\text{DM1}} - (T_{\text{DM1}} - t) \times (f_{\text{cc}} - f_{\text{s}})}{f_{\text{cc}} - f_{\text{dm}}} \quad (3)$$

The parameters f_{cc} , f_{s} , and f_{dm} represent the $f_{\text{Sm}/\text{Nd}}$ values of the average continental crust, the sample, and the depleted mantle, respectively. Specifically, f_{cc} is set at 0.4, f_{dm} is 0.08592, and t signifies the intrusive age of the granite. The calculation for $f_{\text{Sm}/\text{Nd}}$ is derived from the following equation:

$$f_{\text{Sm}/\text{Nd}} = \frac{(^{147}\text{Sm}/^{144}\text{Nd})_{\text{sample}}}{(^{147}\text{Sm}/^{144}\text{Nd})_{\text{CHUR}}} - 1 \quad (4)$$

The two-stage model ages are derived by assuming that the protolith of granitic magmas has a $f_{\text{Sm}/\text{Nd}}$ ratio characteristic of average continental crust. This approach is particularly favored for felsic igneous rocks to account for changes in $f_{\text{Sm}/\text{Nd}}$ ratios that can be induced by geological processes such as partial melting, fractional crystallization, magma mixing, and hydrothermal alteration, among others. Our recalculated data are in close agreement with the original figures. In particular, certain literature sources provide only limited measurements, including values of $\epsilon_{\text{Nd}}(t)$ and T_{DM} , which we have directly incorporated into our research⁵⁸.

- **Metadata Integration.** Drawing a parallel between the acquired data and the metadata of the original article, we began a seamless integration process. This merge links the article's metadata, including author, year, journal, title, volume, page, and DOI, to the table data, laying the groundwork for subsequent manual review and ensuring an impeccable data lineage during the augmentation process.
- **Manual Validation.** As a final step, meticulous manual evaluations are performed to confirm the usability and integrity of the data.

3 Data Records

All collected data presented in this study are available on the Figshare repository: <https://doi.org/10.6084/m9.figshare.24054231.v2>⁵⁹. This data set consists of 12 files. Descriptions of these data records are as follows.

The "Sm-Nd data collection (Automated)" file provides a comprehensive overview of data systematically extracted from the geoscientific literature. Each dataset within this compilation is linked to its primary source through a detailed metadata framework. This framework includes several elements: "Ref. Author" (representing the author of the referenced paper), "Ref. Year" (representing the year of publication), "Ref. Journal" (identifying the publishing journal), "Title" (specifying the title of the referenced article), "Volume" (the specific volume of the publication), "Page" (specifying the exact page of data extraction), and "DOI" (the Digital Object Identifier, a tool that ensures unambiguous source referencing). In addition to this basic data, the automated process also collects specific target data: It collects sample identification ("sample"), geographic coordinates, and location descriptors ("Nation/Region/GeoTectonic Unit/Groups", "Tectonic Unit", "Sub-Tectonic Unit/Sub-Groups", "Longitude", "Latitude"), character attributes, "Latitude", character attributes ("Lithology", "Pluton"), chronological details ("Age(Ma)"), and isotopic measurements ("Sm", "Nd", "¹⁴⁷Sm/¹⁴⁴Nd", "¹⁴³Nd/¹⁴⁴Nd", " 2σ ", "fSm/Nd", " ϵ Nd(t)", "TDM1", "TDM2").

The "Sm-Nd data collection (Annotation)" file encompasses a detailed description of 2,119 manually annotated data points. These have been integrated to enhance our previously established global Sm-Nd dataset. Through meticulous data tracing, we have ensured the completion and validation of all fields. To promote uniformity, we revised the terminologies: "Nation/Region/GeoTectonic unit/Groups" has been standardized to "GeoTectonic unit", while "Subtectonic unit/Sub groups" has been recategorized as "Subtectonic unit". Following a comprehensive recalculation and normalization process, we introduced parameters such as "Calcul. ϵ Nd(0), Recal. ϵ Nd(t), Recalcu. TDM1 (Ga), and Recalcul. TDM2 (Ga)". Drawing upon the foundational historical data labeled "Orig. ϵ Nd(0), Origin ϵ Nd(t), Origi. TDM1 (Ma), and Origi. TDM2 (Ma)", we have transitioned the data nomenclature to "Mapped ϵ Nd(t) and Mapped TDM(Ga)".

The file titled "Table S1a Nd data of Altaids (CAOB) 20230105-4713" consolidates an extensive dataset containing 4,713 entries, detailing the Nd isotopic data of the felsic and intermediate igneous rocks from the Altaids (CAOB). As delineated in prior research, the Altaids is alternately referred to as the Altiid tectonic collage, Central Asian Orogenic Supercollage, Central Asian Fold Belt, or more commonly, the southern Central Asian Orogenic Belt (CAOB). Geographically situated between the Siberian, Baltic (East European Cratons), and Tarim-North China cratons, the Altaids represent the most expansive accretionary orogen globally and are a paramount locus for Phanerozoic crustal growth⁶⁰⁻⁶⁵.

The file "Table S1b Nd data of Cordillera 20220419 1235 data OK new data 20220816" provides a comprehensive dataset comprising 1,235 entries that elucidate the Nd isotopic data of the felsic and intermediate igneous rocks from the North American Cordillera. Spanning over 10,000 km along North America's west coast, the North American Cordillera Orogen stands as a quintessential representation of the Cordilleran (ocean-continent subduction) orogenic system. Its significant expanse and geological features have been foundational in shaping various tectonic and geodynamic theories, making it a paradigmatic example of an accretionary orogen⁶⁶⁻⁷².

The file "Table S1c Nd data of Newfoundland 20220816 418 data OK" presents an exhaustive dataset of 418 entries detailing the Nd isotopic data of the silicic and intermediate igneous rocks from the Newfoundland Appalachians. In North America, the Appalachian Orogen is recognized as a Paleozoic accretion-type orogen. Its formation can be attributed to the accretion and collision of numerous juvenile terranes and ancient blocks, culminating in the significant continent-continent collision between Laurentian and Gondwanan in the Late Permian^{73,74}.

The file "Table S1d Nd data of Lachlan 20220816 411data ok" offers a thorough compilation of 411 entries elucidating the Nd isotopic data of the felsic and intermediate igneous rocks associated with the Lachlan orogen. Situated in Australia, the Lachlan Orogen forms an integral component of the Paleozoic Tasman orogenic system, which extends through eastern Australia and Gondwana. The Thomson Orogen geographically delimits this orogen to the north, the Delamerian Orogen to the west, and the New England Orogen to the east. Its genesis (spanning 450–340 Ma) is attributed to the closure of back-arc basin systems behind a persistent subduction zone symbolized by the New England Fold Belt. Further, its formation involved the accretion of submarine fans, accretionary complexes, extinct volcanic arcs, oceanic crust, and the Tasmanian microcontinent. Conceptually, the Lachlan Orogen is discerned as either a composite accretionary orogen or an extensional accretionary orogen⁷⁵⁻⁷⁸.

The file "Table S1e Nd data of Tethyan Tibet 20220821" provides an exhaustive dataset consisting of 1,576 entries detailing the Nd isotopic values associated with the felsic and intermediate igneous rocks from Tethyan Tibet. This region, known as the Himalaya Orogen, constitutes a significant section of the Tethys. It stands as Earth's preeminent collisional orogen, characterized by its exceptionally thick crust, ranging from 60–85 km, and its remarkable elevation, exceeding 4,000 meters. The genesis of this orogen can be traced back to the India-Asia collision, which commenced between 65–55 Ma. This monumental collision event was preceded by the Mesozoic accretion and collision of various terranes, including but not limited to Songpan, north Qiangtang, south Qiangtang, and Lhasa⁷⁹⁻⁸⁶.

The file "Table S1f Nd data of Caledonides 20220816 302 data ok" offers a comprehensive dataset, encompassing 302 entries that illuminate the Nd isotopic values of the felsic and intermediate igneous rocks from the Caledonides. The Caledonian Orogen, colloquially termed the Caledonides, is manifest in Western Europe, extending as a direct continuum of the Appalachian Mountain chain located in North America. Evidence of orogenic activity is discernible in the northern territories of the British Isles, Scandinavia, Svalbard, eastern Greenland, and specific segments of north-central Europe. The composition of this orogen is intricate, encapsulating numerous terranes rooted in Precambrian foundations—such as the ca. 2.7 Ga Scourian gneiss—and subsequent layering of late Precambrian to early Palaeozoic sediments and volcanic substrates^{87–92}.

The file "Table S1g Nd data of Variscides 1299 20220816" presents an exhaustive dataset, comprising 1,299 entries, which elucidates the Nd isotopic values associated with the felsic and intermediate igneous rocks of the Variscides. The Variscan Orogen, also called the Hercynian Orogen or Variscides, is strategically situated to the south of the Caledonian Orogen, spanning regions of Europe and North Africa. This belt, arising from the Paleozoic-era collision between Gondwana and Laurussia, facilitated the subduction and accretion of various crustal blocks, culminating in the formation of the supercontinent Pangea. The Variscides are emblematic for their juxtaposition of disparate blocks of continental crust and can be interpreted as a continuous accretion of continental crust to Laurussia^{93–96}. As such, the structural and formation dynamics of the Variscides stand in stark contrast to oceanic accretionary orogens, such as the Altai or CAOB.

The file "Table S1h Nd data of Qinling-Dabie 20220816 480 data OK" provides a comprehensive dataset, encompassing 480 entries, that delineates the Nd isotopic values about the felsic and intermediate igneous rocks of the Qinling-Dabie orogen. Situated across central China, the Qinling-Dabie Orogen is a pivotal orogenic structure in Asia. This orogen is composed of four discernible terranes or blocks. Arranged from north to south, these include the North China Block (NCB), the North Qinling Belt (NQB), the South Qinling Belt (SQB), and the South China Block (SCB). These terranes are demarcated by notable geological structures: the Luonan-Luanchuan fault zone and the Shangdan and Mianlue sutures. The genesis of the Shangdan suture can be traced back to the closure of the Shangdan Ocean, a Prototethys offshoot, between 500–420 Ma, while the Mianlue suture emerged due to the closure of the Mianlue Ocean, an offshoot of the Paleotethys, in the interval of 300–220 Ma. Geophysical investigations reveal a notable characteristic of this orogen: the absence of mountain roots and a standard crustal thickness approximating 40 km^{97–101}.

The file "Table S2. Nd Isotopic areas and areal percents of 8 orogens 20220821" provides a systematic representation of the isotopic domains and provinces, detailing both their spatial extents and relative areal percentages across the eight specified orogens.

4 Technical Validation

4.1 Consistency Validation

To maintain the consistency of Sm-Nd data across all orogenic belts, we selected 2,118 entries subjected to human evaluation, and of these, 1,780 entries were validated, resulting in a consistency rate of 84.04%.

Our evaluation was based on three primary criteria:

- We recalibrated the ϵNd values and Nd mode ages employing consistent parameters and juxtaposed them with the values delineated in the original article of¹⁹. Data points were deemed valid if the recalibrated results were closely aligned or were analogous to the original values.
- For samples that incorporated geological information within the table, we executed spatial casts to authenticate the spatial positioning of the orogenic belt. The data was validated upon successful correlation with the location details specified in the article.
- Given that the samples discussed in this study predominantly comprise medium-acidic rocks, it is noteworthy that the $\epsilon\text{Nd}(t)$ values of the 2,118 felsic and intermediate magmatic rocks exhibit a robust linear association with TDM2. This underscores the efficacy of automatic data collection, suggesting its comparability to manually curated data, especially in isotope mapping studies.

4.2 Distribution Validation

In Figures 6, we present a distribution analysis of sample distributions within isotopic domains ($\epsilon\text{Nd}(t)$) contrasted with two-stage Nd-depleted mantle model ages (TDM2). The robustness of our comparative analysis is confirmed by a pronounced linear correlation across eight global orogens, as demonstrated by Wang et al. (2023)⁶. Using a refined and methodologically advanced approach, we have increased the granularity of the data representation, with pronounced improvements observed in geologically complex regions, including the Cordillera, Appalachians, Tethyan Tibet, Variscides, and Qinling-Dabie orogens. Empirical analysis shows an average data improvement of 22.45%, a significant increase that adds resolution and depth to the interpretability of the dataset.

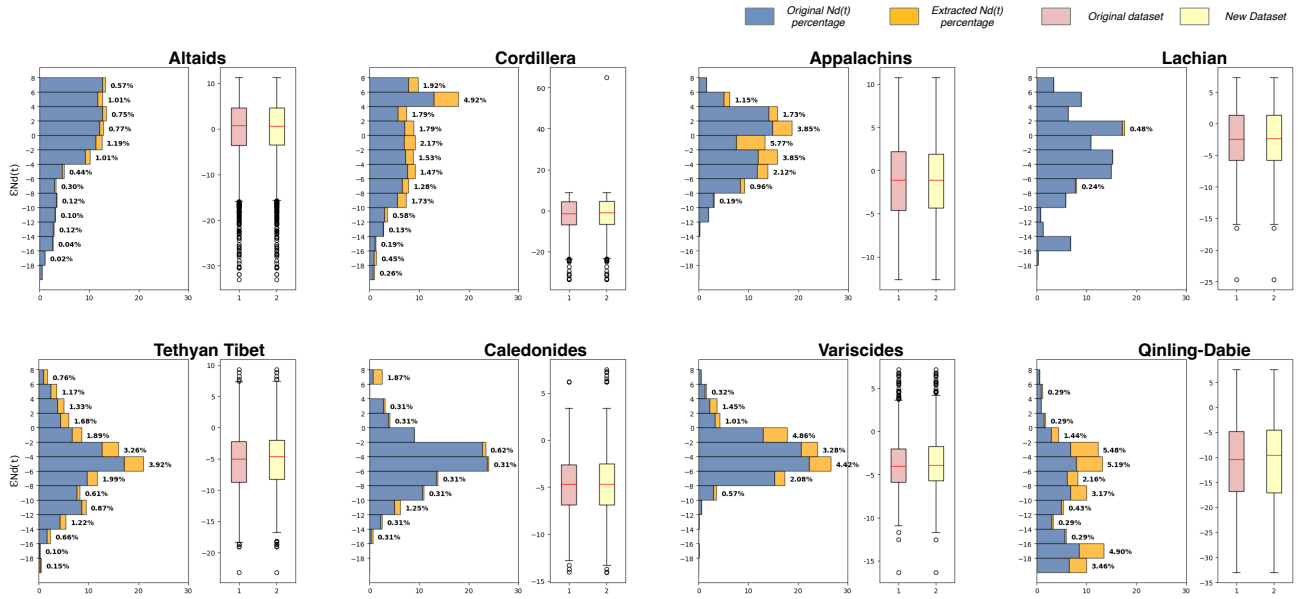


Figure 6. Distribution validation of the original dataset and the dataset obtained through our methodology, illustrating the frequency distribution of ϵ Nd(t) values for the eight orogens. The blue diagram depicts the ϵ Nd(t) percentages from the original dataset, while the orange diagram reflects the percentages from our acquired dataset. In the box plot representation, the pink box delineates the ϵ Nd(t) value distribution of the original dataset, whereas the yellow box characterizes the ϵ Nd(t) value distribution from our newly acquired dataset.

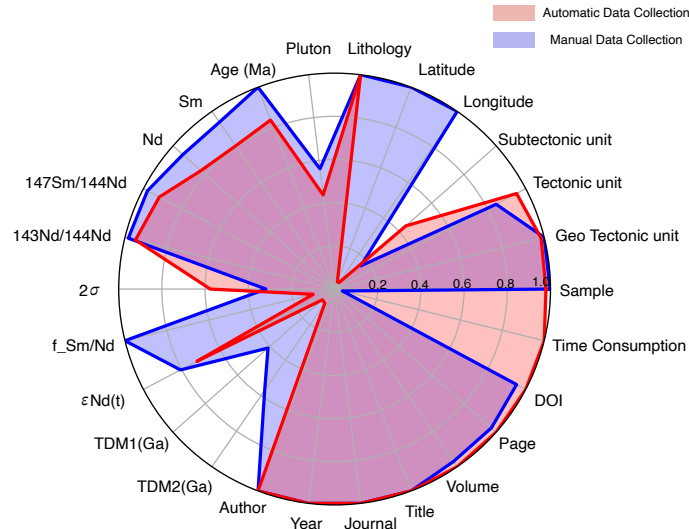


Figure 7. Comparison of data filling rate and time consumption between manual compilation and our automatic data collection method.

4.3 Efficiency Evaluation

As shown in Figure 7, our research delved into an intensive analytical evaluation focused on unraveling the competence of various data collection modalities. Our research juxtaposed automatic and manual data collection techniques and anchored our evaluation on key variables, including time efficiency and data fill rate. This included vital components such as position, attribute, age, sample, and meta-information. Our in-depth comparative analysis revealed marked differences between the two methodologies. One notable observation was the fragmentation of critical data, particularly age and position, interspersed among the various textual and graphical components embedded in the scientific literature. The diverse nature of this information dissemination poses a notable challenge to automatic data extraction, resulting in noticeable variances compared to the precision

and coherence inherent in manual extraction techniques.

However, the extraction of detailed specimen information, mainly associated with sample information, such as tectonic units, is one domain where the precision and speed of automatic mechanisms are strikingly evident. Incorporating an elaborate, carefully curated keyword dictionary enhances the adeptness of automatic extraction, making it faster and significantly more comprehensive. Our focused examination of the temporal dynamics inherent in data extraction and assimilation accentuates an empirical delineation of this enhanced efficiency. To contextualize the time efficiency attributable to our automatic approach, we conducted a comparative analysis, drawing on a dataset comprising 9,000 manually collected and curated Sm-Nd-related records. These records were gleaned utilizing a similar keyword schema as employed in the automatic approach. The findings were illuminating – the manual process was 27 times more time-intensive. This distinction accentuates the functional efficacy of automatic processes, particularly in contexts where the alacrity of data extraction and the integrality of information are paramount. The detailed comparison of data fill rates is illustrated in Table 2.

4.4 Limitations

Throughout our automatic data collection process, we encountered several challenges that called into question the reliability of the automatic data collection process. A predominant challenge was encoding older literature into PDFs via image scanning. This encoding method introduced complexities to data retrieval using traditional PDF parsing techniques. The traditional paradigm for data extraction was firmly rooted in using Optical Character Recognition (OCR) tools. However, the nuances of specific symbols and specialized terms in academic literature tables often led to data misinterpretation by general-purpose OCR tools, compromising the accuracy of data capture.

The landscape of table data definitions presented challenges primarily due to an absence of standardization. This lack necessitated the compilation of an array of header definitions, which, in turn, introduced variability, constraining the efficacy of our automatic table data extraction mechanism from academic literature. Within specific academic disciplines, formulating a targeted keyword list became pivotal, enhancing the efficiency of table data acquisition.

5 Usage Notes

The Sm-Nd isotope dataset provides a valuable resource for studies of orogens, their compositional architecture, and crustal growth patterns^{3,19–24}. This dataset facilitates a nuanced understanding of orogen characterization and categorization^{16–18}. For example, the Nd isotope mapping method, which uses Sm-Nd data in conjunction with age and position information, provides a robust approach to studying crustal growth^{14,15}.^{6,7} presented Nd isotope mapping results from eight emblematic Phanerozoic orogens. Their research delineates the crustal growth patterns inherent to each orogenic belt and introduces an innovative methodology that quantitatively characterizes orogens based on their compositional architecture via isotopic mapping. This method elucidates the intricate relationships between orogenesis and continental growth. In addition, we have pioneered our automated tabular data collection method, which significantly increases the efficiency of data collection and results in a richer, more comprehensive data set.

6 Code Availability

The tabular collection code is available from <https://github.com/sjtugzx/tabularDataCollection>. Instructions for use are available with the code.

References

1. Tarney, J. & Jones, C. Trace element geochemistry of orogenic igneous rocks and crustal growth models. *J. Geol. Soc.* **151**, 855–868 (1994).
2. Condie, K. Growth of continental crust: a balance between preservation and recycling. *Mineral. Mag.* **78**, 623–637 (2014).
3. Cawood, P. A. *et al.* Accretionary orogens through earth history. *Geol. Soc. London, Special Publ.* **318**, 1–36 (2009).
4. Carminati, E., Lustrino, M. & Doglioni, C. Geodynamic evolution of the central and western mediterranean: Tectonics vs. igneous petrology constraints. *Tectonophysics* **579**, 173–192 (2012).
5. Wang, X. *et al.* Quantifying knowledge from the perspective of information structurization. *Plos one* **18**, e0279314 (2023).
6. Wang, T. *et al.* Quantitative characterization of orogens through isotopic mapping. *Commun. Earth & Environ.* **4**, 110 (2023).
7. Wang, T. *et al.* Voluminous continental growth of the altaids and its control on metallogeny. *Natl. Sci. Rev.* (2023).

Keywords	Manual Collection	Our Method
Sample	0.998	0.979
GeoTectonic unit	1.000	0.985
Tectonic unit	0.845	0.952
Subtectonic unit	0.162	0.441
Longitude	1.000	0.036
Latitude	1.000	0.036
Lithology	1.000	1.000
Pluton	0.561	0.439
Age (Ma)	1.000	0.837
Sm	0.939	0.806
Nd	0.939	0.827
$^{147}\text{Sm}/^{144}\text{Nd}$	0.979	0.917
$^{143}\text{Nd}/^{144}\text{Nd}$	0.984	0.950
2σ	0.318	0.576
$f_{\text{Sm}/\text{Nd}}$	1.000	0.102
$\epsilon\text{Nd}(t)$	0.806	0.720
TDM1 (Ga)	0.412	0.075
TDM2 (Ga)	0.570	0.080
Author	1.000	1.000
Year	1.000	1.000
Journal	1.000	1.000
Title	1.000	1.000
Volume	0.970	1.000
Page	0.970	1.000
DOI	0.952	1.000
Average	0.856	0.710

Table 2. Comparative analysis of the filling rate between manual collection and our automatic method across a dataset of 9,000 samples. The best performance are **bold** within each comparison.

8. Green, T., Brunfelt, A. & Heier, K. Rare earth element distribution in anorthosites and associated high grade metamorphic rocks, lofoten-vesteraalen, norway. *Earth Planet. Sci. Lett.* **7**, 93–98 (1969).
9. Pride, C. & Muecke, G. Rare earth element geochemistry of the scourian complex nw scotland—evidence for the granite-granulite link. *Contributions to Mineral. Petrol.* **73**, 403–412 (1980).
10. WASSERBURG, G. Early archean sm-nd model ages from a tonalitic gneiss, northern michigan. *Sel. Stud. Archean Gneisses Low. Proterozoic Rocks, South. Can. Shield.* **182**, 135 (1980).
11. Moorbath, S., Powell, J. L. & Taylor, P. N. Isotopic evidence for the age and origin of the “grey gneiss” complex of the southern outer hebrides, scotland. *J. Geol. Soc.* **131**, 213–222 (1975).
12. Hamilton, P., Evensen, N., O’inions, R. & Tarney, J. Sm—nd systematics of lewisian gneisses: implications for the origin of granulites. *Nature* **277**, 25–28 (1979).
13. Jacobsen, S. B. & Wasserburg, G. Interpretation of nd, sr and pb isotope data from archean migmatites in lofoten-vesteraalen, norway. *Earth Planet. Sci. Lett.* **41**, 245–253 (1978).
14. Gruau, G., Lecuyer, C., Bernard-Griffiths, J. & Morin, N. Origin and petrogenesis of the trinity ophiolite complex (california): new constraints from ree and nd isotope data. *J. Petrol.* 229–242 (1991).
15. Lambert, D. *et al.* Re—os and sm—nd isotope geochemistry of the stillwater complex, montana: implications for the petrogenesis of the jm reef. *J. Petrol.* **35**, 1717–1753 (1994).
16. Dickin, A. Nd isotope mapping of a cryptic continental suture, grenville province of ontario. *Precambrian Res.* **91**, 433–444 (1998).
17. Dickin, A. Crustal formation in the grenville province: Nd-isotope evidence. *Can. J. Earth Sci.* **37**, 165–181 (2000).

18. Wang, T. *et al.* Nd–sr isotopic mapping of the chinese altai and implications for continental growth in the central asian orogenic belt. *Lithos* **110**, 359–372 (2009).
19. Goldstein, S., O’niions, R. & Hamilton, P. A sm-nd isotopic study of atmospheric dusts and particulates from major river systems. *Earth planetary Sci. letters* **70**, 221–236 (1984).
20. Blanchet, C. L. A database of marine and terrestrial radiogenic nd and sr isotopes for tracing earth-surface processes. *Earth Syst. Sci. Data* **11**, 741–759 (2019).
21. Condie, K. C. Preservation and recycling of crust during accretionary and collisional phases of proterozoic orogens: a bumpy road from nuna to rodinia. *Geosciences* **3**, 240–261 (2013).
22. Cawood, P. A., Strachan, R. A., Pisarevsky, S. A., Gladkochub, D. P. & Murphy, J. B. Linking collisional and accretionary orogens during rodinia assembly and breakup: Implications for models of supercontinent cycles. *Earth Planet. Sci. Lett.* **449**, 118–126 (2016).
23. Collins, W. J., Belousova, E. A., Kemp, A. I. & Murphy, J. B. Two contrasting phanerozoic orogenic systems revealed by hafnium isotope data. *Nat. Geosci.* **4**, 333–337 (2011).
24. Collins, W. Hot orogens, tectonic switching, and creation of continental crust. *Geology* **30**, 535–538 (2002).
25. Sudmanns, M. *et al.* Big earth data: disruptive changes in earth observation data management and analysis? *Int. J. Digit. Earth* **13**, 832–850 (2020).
26. Cai, L. & Zhu, Y. The challenges of data quality and data quality assessment in the big data era. *Data science journal* **14**, 2–2 (2015).
27. Ahmed, E. *et al.* The role of big data analytics in internet of things. *Comput. Networks* **129**, 459–471 (2017).
28. Miller, H. J. & Han, J. *Geographic data mining and knowledge discovery* (CRC press, 2009).
29. Chen, H. & Xiao, K. The design and implementation of the geological data acquisition system based on mobile gis. In *2011 19th International Conference on Geoinformatics*, 1–6 (IEEE, 2011).
30. Last, W. M. & Smol, J. P. *Tracking environmental change using lake sediments: volume 2: physical and geochemical methods*, vol. 2 (Springer Science & Business Media, 2002).
31. Sarbas, B. The georoc database as part of a growing geoinformatics network. In *Geoinformatics 2008—data to knowledge*, 42–43 (USGS, 2008).
32. Gard, M., Hasterok, D. & Halpin, J. A. Global whole-rock geochemical database compilation. *Earth Syst. Sci. Data* **11**, 1553–1566 (2019).
33. Ren, S., He, K., Girshick, R. & Sun, J. Faster r-cnn: Towards real-time object detection with region proposal networks. *Adv. neural information processing systems* **28** (2015).
34. He, K., Gkioxari, G., Dollár, P. & Girshick, R. Mask r-cnn. In *Proceedings of the IEEE international conference on computer vision*, 2961–2969 (2017).
35. Redmon, J. & Farhadi, A. Yolov3: An incremental improvement. *arXiv preprint arXiv:1804.02767* (2018).
36. Garncarek, Ł. *et al.* Lambert: Layout-aware language modeling for information extraction. In *Document Analysis and Recognition—ICDAR 2021: 16th International Conference, Lausanne, Switzerland, September 5–10, 2021, Proceedings, Part I*, 532–547 (Springer, 2021).
37. Yu, W., Lu, N., Qi, X., Gong, P. & Xiao, R. Pick: processing key information extraction from documents using improved graph learning-convolutional networks. In *2020 25th International Conference on Pattern Recognition (ICPR)*, 4363–4370 (IEEE, 2021).
38. Xu, Y. *et al.* Layoutlm: Pre-training of text and layout for document image understanding. In *Proceedings of the 26th ACM SIGKDD International Conference on Knowledge Discovery & Data Mining*, 1192–1200 (2020).
39. Zhang, P. *et al.* Trie: end-to-end text reading and information extraction for document understanding. In *Proceedings of the 28th ACM International Conference on Multimedia*, 1413–1422 (2020).
40. Rahman, W. *et al.* Integrating multimodal information in large pretrained transformers. In *Proceedings of the conference. Association for Computational Linguistics. Meeting*, vol. 2020, 2359 (NIH Public Access, 2020).
41. Cervato, C. *et al.* The chronos system: geoinformatics for sedimentary geology and paleobiology. In *2005 IEEE International Symposium on Mass Storage Systems and Technology*, 182–186 (IEEE, 2005).

42. Snyder, W., Lehnert, K., Ito, E., Harms, U. & Klump, J. Geoscinet: Building a global geoinformatics partnership. In *AGU Fall Meeting Abstracts*, vol. 2008, IN31D–03 (2008).
43. Zhang, C. *et al.* Geodeepdive: statistical inference using familiar data-processing languages. In *Proceedings of the 2013 ACM SIGMOD International Conference on Management of Data*, 993–996 (2013).
44. Khan, A., Kim, T., Byun, H. & Kim, Y. Scispace: A scientific collaboration workspace for geo-distributed hpc data centers. *Futur. Gener. Comput. Syst.* **101**, 398–409 (2019).
45. Zhang, S. *et al.* Geodeepshovel: A platform for building scientific database from geoscience literature with ai assistance. *Geosci. Data J.* (2022).
46. Niu, X. An ontology driven relational geochemical database for the earth’s critical zone: Czchemdb. *J. Environ. Informatics* **23** (2014).
47. Walker, J., Lehnert, K., Hofmann, A., Sarbas, B. & Carlson, R. Earthchem: International collaboration for solid earth geochemistry in geoinformatics. In *AGU Fall Meeting Abstracts*, vol. 2005, IN44A–03 (2005).
48. Boone, S. C. *et al.* Ausgeochem: An open platform for geochemical data preservation, dissemination and synthesis. *Geostandards Geoanalytical Res.* **46**, 245–259 (2022).
49. Rodriguez-Corcho, A. F. *et al.* The colombian geochronological database (cgd). *Int. Geol. Rev.* **64**, 1635–1669 (2022).
50. Tkaczyk, D., Szostek, P., Fedoryszak, M., Dendek, P. J. & Bolikowski, Ł. Cermine: automatic extraction of structured metadata from scientific literature. *Int. J. on Document Analysis Recognit. (IJ DAR)* **18**, 317–335 (2015).
51. Girshick, R. Fast r-cnn. In *Proceedings of the IEEE international conference on computer vision*, 1440–1448 (2015).
52. Li, M. *et al.* Tablebank: Table benchmark for image-based table detection and recognition. In *Proceedings of the Twelfth Language Resources and Evaluation Conference*, 1918–1925 (2020).
53. Jeeva, C. *et al.* Intelligent image text reader using easy ocr, nrclex & nltk. In *2022 International Conference on Power, Energy, Control and Transmission Systems (ICPECTS)*, 1–6 (IEEE, 2022).
54. Jacobsen, S. & Wasserburg, G. Sm-nd isotopic evolution of chondrites and achondrites, ii. *Earth Planet. Sci. Lett.* **67**, 137–150 (1984).
55. White, W. M. & Hofmann, A. W. Sr and nd isotope geochemistry of oceanic basalts and mantle evolution. *Nature* **296**, 821–825 (1982).
56. Peucat, J., Vidal, P., Bernard-Griffiths, J. & Condie, K. Sr, nd, and pb isotopic systematics in the archean low-to high-grade transition zone of southern india: syn-accretion vs. post-accretion granulites. *The J. Geol.* **97**, 537–549 (1989).
57. DePaolo, D. J. & Wasserburg, G. Nd isotopic variations and petrogenetic models. *Geophys. research letters* **3**, 249–252 (1976).
58. Keto, L. S. & Jacobsen, S. B. Nd and sr isotopic variations of early paleozoic oceans. *Earth Planet. Sci. Lett.* **84**, 27–41 (1987).
59. Guo, Z. *et al.* Sm-nd isotope data compilation from geoscientific literature. *figshare* <https://doi.org/10.6084/m9.figshare.24054231.v2> (2023).
60. Şengör, A., Natal’In, B. & Burtman, V. Evolution of the altaid tectonic collage and palaeozoic crustal growth in eurasia. *Nature* **364**, 299–307 (1993).
61. Şengör, A. C., Natal’in, B. A., Sunal, G. & van der Voo, R. The tectonics of the altaids: Crustal growth during the construction of the continental lithosphere of central asia between 750 and 130 ma ago. *Annu. Rev. Earth Planet. Sci.* **46**, 439–494 (2018).
62. Sengör, A. C. & Natal’In, B. A. Turcic-type orogeny and its role in the making of the continental crust. *Annu. Rev. Earth Planet. Sci.* **24**, 263–337 (1996).
63. Şengör, A. C., Sunal, G., Natal’in, B. A. & van der Voo, R. The altaids: A review of twenty-five years of knowledge accumulation. *Earth-Science Rev.* **228**, 104013 (2022).
64. Yakubchuk, A. Evolution of the central asian orogenic supercollage since late neoproterozoic revised again. *Gondwana Res.* **47**, 372–398 (2017).
65. Mossakovsky, A. Central asian fold belt: geodynamic evolution and formation history. *Geotectonics* **24**, 445–474 (1994).
66. Burchfiel, B. & Davis, G. A. Nature and controls of cordilleran orogenesis, western united states: Extensions of an earlier synthesis. *Am. J. Sci.* **275**, 363–396 (1975).

67. DeCelles, P. G. Late jurassic to eocene evolution of the cordilleran thrust belt and foreland basin system, western usa. *Am. J. Sci.* **304**, 105–168 (2004).
68. DeCelles, P. G., Ducea, M. N., Kapp, P. & Zandt, G. Cyclicity in cordilleran orogenic systems. *Nat. Geosci.* **2**, 251–257 (2009).
69. Dickinson, W. R. Evolution of the north american cordillera. *Annu. Rev. Earth Planet. Sci.* **32**, 13–45 (2004).
70. Yonkee, W. A. & Weil, A. B. Tectonic evolution of the sevier and laramide belts within the north american cordillera orogenic system. *Earth-Science Rev.* **150**, 531–593 (2015).
71. Fitz-Díaz, E., Lawton, T. F., Juárez-Arriaga, E. & Chávez-Cabello, G. The cretaceous-paleogene mexican orogen: Structure, basin development, magmatism and tectonics. *Earth-Science Rev.* **183**, 56–84 (2018).
72. Chapman, J. B. *et al.* The north american cordilleran anatectic belt. *Earth-Science Rev.* **215**, 103576 (2021).
73. Williams, H. Appalachian orogen in canada. *Can. J. Earth Sci.* **16**, 792–807 (1979).
74. Williams, H., Colman-Sadd, S. & Swinden, H. Tectonic-stratigraphic subdivisions of central newfoundland. *Curr. Res. Part B. Geol. Surv. Canada, Pap.* **88**, 91–98 (1988).
75. Foster, D. A. & Gray, D. R. Evolution and structure of the lachlan fold belt (orogen) of eastern australia. *Annu. Rev. Earth Planet. Sci.* **28**, 47–80 (2000).
76. Glen, R., Crawford, A., Percival, I. & Barron, L. Early ordovician development of the macquarie arc, lachlan orogen, new south wales. *Aust. J. Earth Sci.* **54**, 167–179 (2007).
77. Foster, D. A., Gray, D. R., Spaggiari, C., Kamenov, G. & Bierlein, F. P. Palaeozoic lachlan orogen, australia; accretion and construction of continental crust in a marginal ocean setting: isotopic evidence from cambrian metavolcanic rocks. *Geol. Soc. London, Special Publ.* **318**, 329–349 (2009).
78. Collins, W. Evaluation of petrogenetic models for lachlan fold belt granitoids: implications for crustal architecture and tectonic models. *Aust. J. Earth Sci.* **45**, 483–500 (1998).
79. Yin, A. & Harrison, T. M. Geologic evolution of the himalayan-tibetan orogen. *Annu. review earth planetary sciences* **28**, 211–280 (2000).
80. Tilmann, F., Ni, J. & Team, I. I. S. Seismic imaging of the downwelling indian lithosphere beneath central tibet. *Science* **300**, 1424–1427 (2003).
81. Van Hinsbergen, D. J. *et al.* Greater india basin hypothesis and a two-stage cenozoic collision between india and asia. *Proc. Natl. Acad. Sci.* **109**, 7659–7664 (2012).
82. Xu, Z. *et al.* Orogen-parallel ductile extension and extrusion of the greater himalaya in the late oligocene and miocene. *Tectonics* **32**, 191–215 (2013).
83. Xu, Z.-Q. *et al.* Crustal structure of the indus–tsangpo suture zone and its ophiolites in southern tibet. *Gondwana Res.* **27**, 507–524 (2015).
84. Xiao, W. New paleomagnetic data confirm a dual-collision process in the himalayas. *Natl. Sci. Rev.* **2**, 395–396 (2015).
85. Xiao, W. *et al.* Anatomy of composition and nature of plate convergence: Insights for alternative thoughts for terminal india-urasia collision. *Sci. China Earth Sci.* **60**, 1015–1039 (2017).
86. Hou, Z. *et al.* A genetic linkage between subduction-and collision-related porphyry cu deposits in continental collision zones. *Geology* **43**, 247–250 (2015).
87. Cartwright, I. & Barnicoat, A. Evolution of the scourian complex. *Geol. Soc. London, Special Publ.* **43**, 297–301 (1989).
88. Frost, C. & NIONS, R. O. Caledonian magma genesis and crustal recycling. *J. Petrol.* **26**, 515–544 (1985).
89. McKerrow, W., Mac Niocaill, C. & Dewey, J. The caledonian orogeny redefined. *J. Geol. society* **157**, 1149–1154 (2000).
90. Van Staal, C., Dewey, J., Niocaill, C. M. & McKerrow, W. The cambrian-silurian tectonic evolution of the northern appalachians and british caledonides: history of a complex, west and southwest pacific-type segment of iapetus. *Geol. Soc. London, Special Publ.* **143**, 197–242 (1998).
91. Torsvik, T. *et al.* Continental break-up and collision in the neoproterozoic and palaeozoic—a tale of baltica and laurentia. *Earth-Science Rev.* **40**, 229–258 (1996).
92. Oliver, G. J. Reconstruction of the grampian episode in scotland: its place in the caledonian orogeny. *Tectonophysics* **332**, 23–49 (2001).

93. Matte, P. Accretionary history and crustal evolution of the variscan belt in western europe. *Tectonophysics* **196**, 309–337 (1991).
94. Kroner, U. & Romer, R. L. Two plates—many subduction zones: the variscan orogeny reconsidered. *Gondwana Res.* **24**, 298–329 (2013).
95. Stampfli, G., Hochard, C., Vérard, C., Wilhem, C. *et al.* The formation of pangea. *Tectonophysics* **593**, 1–19 (2013).
96. Laurent, O. *et al.* Protracted, coeval crust and mantle melting during variscan late-orogenic evolution: U–pb dating in the eastern french massif central. *Int. J. Earth Sci.* **106**, 421–451 (2017).
97. Mattauer, M. *et al.* Tectonics of the qinling belt: build-up and evolution of eastern asia. *Nature* **317**, 496–500 (1985).
98. Meng, Q.-R. & Zhang, G.-W. Timing of collision of the north and south china blocks: controversy and reconciliation. *Geology* **27**, 123–126 (1999).
99. Zhang, G., Zhang, B., Yuan, X. C., Xiao, Q. *et al.* Qinling orogenic belt and continental dynamics (2001).
100. Dong, Y. & Santosh, M. Tectonic architecture and multiple orogeny of the qinling orogenic belt, central china. *Gondwana Res.* **29**, 1–40 (2016).
101. Meng, Q.-R. & Zhang, G.-W. Geologic framework and tectonic evolution of the qinling orogen, central china. *Tectonophysics* **323**, 183–196 (2000).

7 Author contributions statement

Zhixin Guo: Conceptualization (equal); methodology (equal); software (equal); validation (lead); writing - original draft (lead). Tao Wang: Conceptualization (equal); data validation (equal). Chaoyang Wang: Conceptualization (equal); data validation (equal). Jianping Zhou: Software (equal); writing - review and editing (equal). Guanjie Zheng: Conceptualization (equal); formal analysis (equal); methodology (equal); project administration (equal); supervision (lead); writing - review and editing (equal). Xinbing Wang: Project administration (equal); supervision (equal). Chenghu Zhou: Project administration (equal).

8 Competing interests

The authors declare no competing interests.